The Japan Society
of Applied Physics

PROGRESS REVIEWS

Optical and thermal designs of near field transducer for heat assisted magnetic recording

View the article online for updates and enhancements.

Related content

CrossMark

Optical and thermal designs of near field transducer for heat assisted magnetic recording

Anurup Datta and Xianfan Xu*

School of Mechanical Engineering and Birck Nanotechnology Center, Purdue University, West Lafayette, IN 47906, U.S.A.

*E-mail: xxu@ecn.purdue.edu

Heat assisted magnetic recording (HAMR) is considered one of the new generation hard drive recording technologies for increasing the data storage density. At its core, HAMR devices are dependent on plasmonic nano antennas, called near field transducers (NFT) to locally deliver heat to storage media. Hence, the design of NFT is crucial for an optimized HAMR device. Several types of NFT designs have been studied through optical and thermal simulations and are quantified using appropriate figures of merit. In addition, the possibility of exciting NFTs at a longer wavelength (1550 nm) has been studied, and it is found that there is a significant improvement of the thermal performance. The effect of having tapers in the geometry of the NFT and their role in improving the NFT thermal performance are also discussed. These studies point to different directions that performance of NFT can be improved. © 2018 The Japan Society of Applied Physics

1. Introduction

With the rapid growth in the amount of digital data worldwide, it is necessary for the hard drive industry to find ways to increase the capacities of hard drives. With the current recording technology for data storage which is primarily the perpendicular magnetic recording, a maximum areal data density of about 500 Gbits/in.^{2} is achievable. However, further attempts to increase the areal data density by reducing the grain size is not practical due to the super paramagnetic limit of the medium.[1] The superparamagnetic limit relates to the equation given by

$$\frac{K_{\mathrm{u}}V}{k_{\mathrm{b}}T} > 70, \tag{1}$$

where K_{u} is the magnetic anisotropy, V is the volume of the grain, k_{b} is the Boltzmann constant, and T is the temperature. Equation (1) states that the total energy associated with the magnetic anisotropy of the medium must be at least 70 times greater than the thermal energy of the medium for a good signal to noise ratio. The volume of the grain, V must be reduced for high density data storage and hence the superparamagnetic limit condition can only be fulfilled by increasing the magnetic anisotropy of the recording medium. However, increasing the magnetic anisotropy is also associated with the rise of the required switching magnetic field of the medium for the write cycle which is not feasible with the current hard drive head technology. Heat assisted magnetic recording (HAMR) technology addresses this issue by locally raising the temperature of the recording medium[2–6] which in turn allows the data to be written in the magnetic recording medium with the available amount of the magnetic field in the recording head. After the write process, the medium again cools down to the room temperature, where the medium is more thermally stable and the data is stored at room temperature. It is assumed that HAMR can successfully scale the areal data densities to 1 Tbits/in.^{2} and beyond. Figure 1 shows the projected growth of the areal data densities over time and the associated technologies to achieve that growth.[7]

The primary goal of HAMR is to achieve high density data recording and for that purpose, the temperature rise in the medium must be confined to a very tiny volume, which is
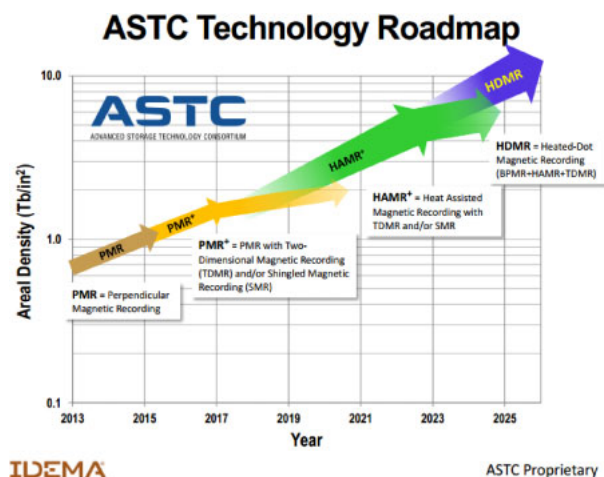

Fig. 1. (Color online) Figure showing the growth of areal data densities over time and the various projected technologies to meet the areal data density targets (source: Ref. 7).

much beyond the diffraction limit of light if light is used as heating source. Hence, conventional ways to focus light in the medium by diffractive optics and heat it, fails to achieve this resolution. HAMR system uses instead, the plasmonic capabilities of a metallic nano-antenna, also known as near field transducer (NFT) and utilizes the localized surface plasmons to concentrate and focus light to such a small volume.[8–11] An external laser source is coupled to a waveguide which then transports the incident energy from the laser to the NFT.[12] The NFT when excited with its working wavelength of light, can generate very strong field intensity over an area of tens of nanometers.

It is understandable that the performance of a HAMR device depends strongly on the design of its underlying NFT. The structure of the NFT should be such that it enables a very high field concentration at its apex. This is achieved by several approaches including: 1) making the structure resonant at a particular wavelength; 2) utilizing the "lightning rod" effect, which essentially relies on the fact that the electric field concentrates along the sharp tips or notches in the geometric design; and 3) by efficient use of an image dipole.[13,14] Some functional NFT designs include the
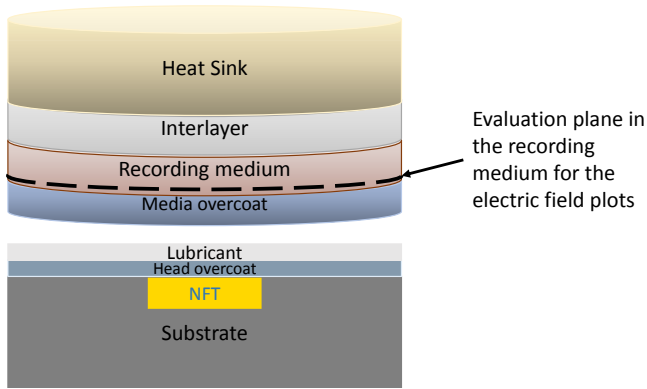
Fig. 2. (Color online) Different layers in the media stack used in the simulation model. The dashed line within the recording medium shows the plane where the electric fields are calculated in Figs. 3 and 5.

triangular antenna,[13,15] E antenna,[16] lollipop structure,[17] bowtie aperture,[18,19] C-aperture,[20,21] and nanobeak antenna.[22,23] Increasing the efficiency of the coupling of the incident laser power to the recording medium is one of the primary goals in designing a better NFT.

The operation of an NFT is also associated with the self-heating of the NFT due to the intrinsic lossy nature of the plasmonic metals at the excitation wavelengths of the NFT. This unwanted temperature rise of the NFT due to self heating can be severely detrimental to the functionality of the NFT causing reliability issues.[24–29] Hence the temperature profile of the NFT during the operation of a HAMR system is another critical factor which should be considered while designing an NFT. This paper details and reviews some of the strategies and methods to improve upon the existing performance of the several NFT designs. Several figures of merit, both optical and thermal will be described based on which the NFT performance can be quantified. The performance of several existing and common NFT designs in the literature will be reviewed and elaborated first. It is found out that the introduction of a taper in the geometry of the NFT and changing the working wavelength of the NFT excitation to longer wavelength can improve the thermal performance of the NFT, especially in helping to reduce the peak temperature rise of the NFT compared to the peak temperature rise of the recording medium.

2. Optical and thermal modeling of NFTs and figures of merit

Coupled full wave electromagnetic and thermal simulations were performed using ANSYS HFSS and Workbench respectively. The simulation model with layers of different materials in the recording medium side is shown in Fig. 2. The recording medium is considered to be made of FePt-C nanocomposite films which has a nominal grain diameter of 15 and 9.1 nm in height.[30] The effects of grains and boundaries were considered in the simulation through the use of anisotropic thermal conductivity (lateral conductivity = 1.5 W m^{-1} K^{-1} and vertical conductivity = 7 W m^{-1} K^{-1}). The media is coated on a substrate generally made of a dielectric material such as glass while the NFT made of gold remains embedded in a substrate like Al$_2$O$_3$ or SiO$_2$ (which has an isotropic thermal conductivity of 1 W m^{-1} K^{-1}, density of 2650 kg/m^3, specific heat of 700

J kg^{-1} K^{-1} and a refractive index of 1.5). Additional details about the simulation setup and the optical and thermal properties of the different layers can be found elsewhere.[31,32]

The absorption in the recording medium and the NFT can be calculated by the power dissipated and is given according to[18]

$$q''' = \frac{1}{2} \varepsilon_0 \omega \, \text{Im}(\varepsilon) |E|^2, \tag{2}$$

where ε_0 is the free space permittivity, ω is the angular frequency of the light, ε is the complex relative permittivity of the gold, and $|E|$ is the electric field. A Gaussian laser beam of power 5 mW focused to a spot size of 0.3 μm is considered. In the coupled thermal simulations, the power absorbed in the recording medium and the NFT per unit volume is taken as the heat generation term, q''' and the temperature T is calculated from the underlying heat diffusion equation:

$$\rho c \frac{\partial T}{\partial t} = \frac{\partial}{\partial x}\left(k_x \frac{\partial T}{\partial x}\right) + \frac{\partial}{\partial y}\left(k_y \frac{\partial T}{\partial y}\right)$$
$$+ \frac{\partial}{\partial z}\left(k_z \frac{\partial T}{\partial z}\right) + q''', \tag{3}$$

where ρ is the density of the control element, c is its specific heat, and k_x, k_y, and k_z are the thermal conductivities of the control element in x-, y-, and z-direction, respectively.

Transient thermal simulations were performed wherein the temperature of the recording medium was considered at the end of 1 ns and the temperature of the NFT was considered at the steady state.

2.1 Optical figures of merit

The optical figures of merit that have been used for the quantification of the NFT performance are namely, coupling efficiency and spot size. In short, the coupling efficiency is defined as the power absorbed in the recording medium within a disk of diameter 70 nm divided by the net incident power on the NFT while the spot size refers to the full width at half maximum (FWHM) of the spot in the recording medium.

2.2 Thermal figures of merit

The thermal figures of merit that have been used are $\Delta T_{\text{medium}}/\Delta T_{\text{NFT}}$, the thermal spot size, the thermal gradient and $\Delta T_{\text{medium}}/P_{\text{incident}}$.

- $\Delta T_{\text{medium}}/\Delta T_{\text{NFT}}$ denotes the peak temperature rise of the recording medium to the peak temperature rise of the NFT. Here the peak temperature rise of the recording medium is considered at the end of 1 ns while the peak temperature rise of the NFT is considered at the steady state. Higher number for this figure of merit indicates greater medium temperature rise for low NFT self-heating.
- Thermal spot size is the full width at half maximum (FWHM) of the temperature profile at the recording medium at the end of 1 ns.
- Thermal gradient is the temperature change per unit length is calculated at a location which is 20 K less than the peak temperature at the recording medium. Greater thermal gradients are preferred in the recording medium which will eliminate long thermal tails. The thermal gradients can be defined in the down track and cross track directions.
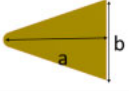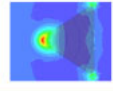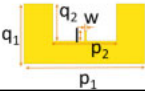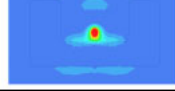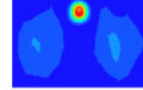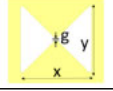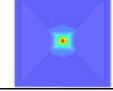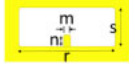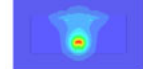
	NFT	Electric field plot at the recording medium	Coupling efficiency	Spot size
Triangle antenna			2.7 %	28nm x 40nm
E antenna			5.8 %	32nm x 36nm
Lollipop antenna			3.5 %	52nm x 62nm
Bowtie aperture			3.2 %	36nm x 44nm
C aperture			2.6 %	32nm x 34nm

Fig. 3. (Color online) Comparative performances of different NFT designs.

- $\Delta T_{\text{medium}}/P_{\text{incident}}$ denotes the overall thermal efficiency of the NFT system and is given by the temperature rise of the medium per unit incident power.

3. Performance of different types of NFTs

Out of the different plasmonic antenna designs that could be suitable for HAMR application, several of them have been studied for their use as an NFT transducer such as the triangle antenna, the E-antenna, the lollipop antenna, the bowtie antenna, the C aperture among others. While a detailed description of each of these antennas is available in the literature, a relative comparison between the performance of several of these antennas is presented here based on similar simulation environment. Obviously, for any plasmonic antennas, their performance depends significantly on their geometric dimensions.[33,34] Hence the comparative analysis between the antennas should include a parametric study for each design which tends to optimize a figure of merit for that design. In this work, the coupling efficiency is chosen as the figure of merit which is maximized by varying the geometric parameters for each of the antenna design. The minimum feature size in each of these simulations is restricted to 20 nm for practical considerations.

The optical performance of several of the antennas is summarized in Fig. 3 which also provides the relevant dimensions, the electric field plot, the coupling efficiency and the spot size in the recording medium. The electric fields are calculated within the recording medium at the interface of the media overcoat and the recording medium as shown by the dashed line in Fig. 2.

For the triangle antenna, an optimized value of $a = 150$ nm, $b = 200$ nm, and $t = 80$ nm (where t is the thickness of the film) gives a coupling efficiency of 2.7% and a spot size of 28×40 nm^2 at a wavelength of 800 nm. The triangular antenna has not only one strong hotspot at the apex but also two tiny hotspots near the base of the triangle. The E antenna which consists of the notch as well as the wings and the body for enforcing the resonance condition at a particular wavelength (850 nm in this case) has an optimized dimension of $w = 20$ nm, $l = 50$ nm, $p_1 = 600$ nm, $p_2 = 316$ nm, $q_1 = 300$ nm, and $q_2 = 186$ nm. A coupling efficiency of 5.8% and a spot size of 32×36 nm^2 is obtained. The lollipop antenna consists of a circular metallic disc and a peg attached to it at one side. The dimensions of $d = 190$ nm, $P_1 = 20$ nm, $P_w = 20$ nm, $t = 35$ nm at 830 nm incident wavelength gives the maximum coupling efficiency of 3.5%. This generates a spot size of 44×51 nm^2 in the recording medium.

Unlike the previous three NFT designs, bowtie aperture is an aperture based NFT consisting of two triangular arms with a small gap in between them. The gap, g is considered to be 20 nm in the simulation model. The bowtie aperture acts as a ridge waveguide. At 800 nm wavelength, dimensions of $x = 400$ nm and $y = 400$ nm with a thickness of 90 nm generates a coupling efficiency of 3.2% and a spot size of 36×44 nm^2. The C-aperture is another aperture based ridge waveguide-like NFT which consists of a rectangular window in a metal film with a notch for field concentration. The aperture portion resembles the C shape. At 800 nm wavelength, $s = 100$ nm, $r = 250$ nm, $m = 20$ nm, $n = 30$ nm and thickness of 100 nm gives a coupling efficiency of 2.6% and a spot size of 32×34 nm^2. From Fig. 3, we find that the E antenna is one of the best in terms of the coupling efficiency into the recording medium.

The thermal figures of merit for different NFT designs are provided in Table I. We see that aperture based NFTs such as the bowtie aperture and the C-aperture perform much better when the figure of merit $\Delta T_{\text{medium}}/\Delta T_{\text{NFT}}$ is considered. For the aperture based NFTs, the heat that is accumulated at the tip of the NFT can quickly diffuse over a larger area within the metal film due to the high thermal conductivity of the film. This leads to a low rise in the NFT peak temperature. While the trend of the temperature rise per unit power is very closely related to the coupling efficiency across the different designs, the differences in the thermal spot size across the different designs is related to both the optical spot size and the shape of the spot. It is also seen that generally a higher temperature rise per power also leads to larger thermal gradients.

Table I.   Thermal figures of merit for different NFTs.

| NFT design	$\Delta T_{\text{medium}}/\Delta T_{\text{NFT}}$	Thermal spot size (nm^2)	Temperature rise per unit power (K/mW)	Thermal gradient (K/nm)	
				Cross-track	Down track
Triangle antenna	0.87	63×76	68.6	3.3	5.2
E antenna	1.83	76×89	124.3	7.55	6.46
Lollipop antenna	1.24	65×71	82.4	3.7	3.14
Bowtie aperture	25.4	54×68	82.8	4.38	5.44
C-aperture	26	64×76	67.8	4.1	4.4
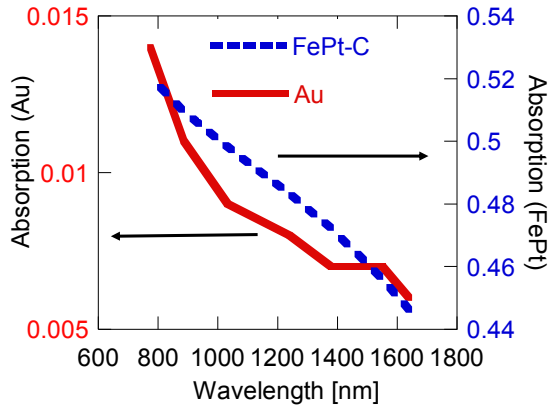
Fig. 4.   (Color online) Absorptivity versus wavelength for Au and recording medium (FePt-C).

4.   Strategies for improved NFT performance

4.1   Effect of change of working wavelength

In this section, we explore an alternate way of reducing the temperature rise of the NFT by changing the excitation wavelength of the plasmonic structures to longer wavelengths. In the longer wavelength range, the absorptivity of gold decreases more rapidly than that of the recording medium as shown in Fig. 4. For calculating the absorptivity data, the gold optical constants are taken from Johnson and Christy[35] and the wavelength dependent FePt-C optical constants are taken from Cen et al.[30] It is seen from Fig. 4 that, the absorptivity of gold decreases by about 300% as we move from 800 to 1550 nm while the absorptivity of FePt-C decreases by only 20%. Hence, we expect an appreciable decrease in NFT self-heating at longer wavelengths. We compare the performance of NFT which is optimized near 800 nm versus NFT optimized at 1550 nm to illustrate the effect of longer working wavelengths. We demonstrate the effect of longer wavelength by studying two NFT designs, the triangle antenna and the E antenna.

First, we choose two triangle NFT designs, one resonant at 800 nm (dimensions: $a = 150$ nm, $b = 200$ nm, $t = 80$ nm) with a coupling efficiency of 2.7% and another resonant at 1550 nm (dimensions: $a = 220$ nm, $b = 150$ nm, $t = 80$ nm) with a coupling efficiency of 2.6%. The top view of the electric field profile at the recording medium and the cross sectional electric field across the substrate and the NFT is shown in Fig. 5. Figures 5(a) and 5(b) show the field profile corresponding to the triangle designs at 850 and 1550 nm, respectively. From Fig. 5(a) it is seen that, the field in the recording medium has only one region of field concentration near the tip of the antenna. On the other hand, at 1550 nm, a higher order plasmonic mode gets excited which has an
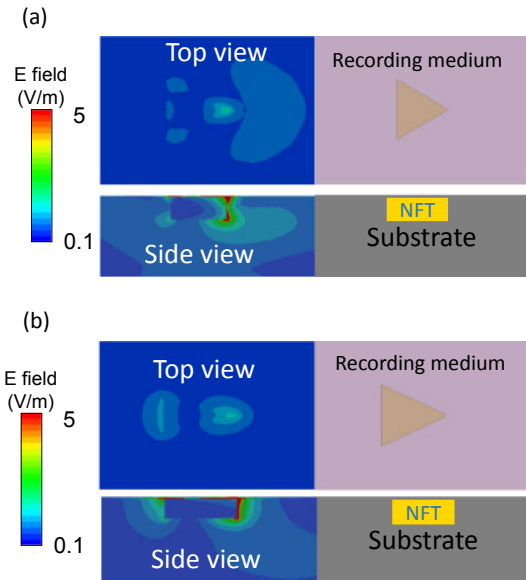

Fig. 5.   (Color online) (a) Electric field plot at the surface of the recording medium (top view) and the cross sectional electric field (side view) at (a) 800 nm and (b) 1550 nm. The sectional views of the structural model are shown to the right of the field plots.

additional charge concentration near the base of the triangle, as is shown in Fig. 5(b). From the electric field profiles, it can be inferred that two different plasmonic modes are excited in the triangle antenna at 800 nm and at 1550 nm.[32] It is found that with the increase in wavelength to 1550 nm, the optical spot size in the recording medium increases to 42×52 nm^2 compared to 28×40 nm^2 at a wavelength of 800 nm, but at the same time, the absorption percentage for the NFT at 1550 nm decreases to 2.6% compared to that for the NFT at 800 nm which is 9.1%. This shows a significant reduction in the power absorbed by the NFT at longer wavelengths which can reduce the NFT self-heating drastically.

The results of the thermal simulations for the triangle antennas illuminated with two different wavelengths are provided in Table II. The temperature rise in the medium is almost similar due to the coupling efficiency being almost the same. However, the maximum steady state temperature rise for the NFT at 800 nm is 390 K while the maximum temperature rise at 1550 nm is only 148 K. Thus the thermal figure of merit ($\Delta T_{\text{medium}}/\Delta T_{\text{NFT}}$) at 800 nm is 0.87 while that at 1550 nm is 2.09, about a 2.38 times increase. The full width at half maxima (FWHM) thermal spot size at the recording medium is 63×76 nm^2 at 800 nm while it is 97×108 nm^2 at 1550 nm. The increase in thermal spot size is primarily related to the increased optical spot size at 1550 nm. Figure 6 shows the temporal temperature rise of the triangle

Table II. Table comparing the thermal performance of triangle antenna NFTs at 800 and 1550 nm.

| Thermal figures of merit	Triangle antenna resonant at 800 nm	Triangle antenna resonant at 1550 nm
$\Delta T_{medium}/\Delta T_{NFT}$	0.87	2.09
Thermal spot size (nm^2)	63×76	97×108
Thermal gradient (K/nm)	5.2: down track	2.4: down track
	3.3: cross track	1.73: cross track
$\Delta T_{medium}/P_{incident}$ (K/mW)	68.6	62.2
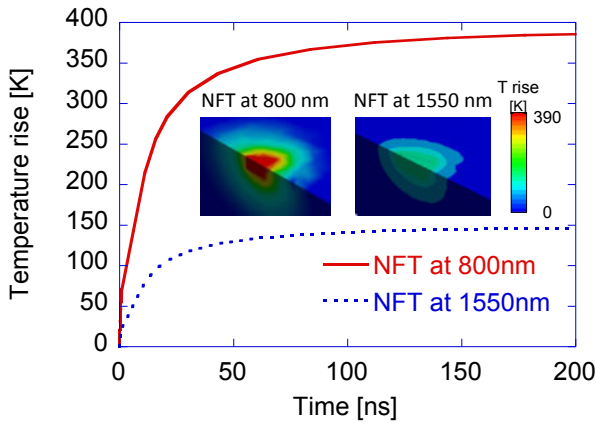
Fig. 6. (Color online) Temporal rise of the peak temperature of the triangle NFTs at 800 and 1550 nm. Inset shows the cross sectional temperature profiles of the NFT.

Table III. Table comparing the thermal performance of E antenna NFTs at 850 and 1550 nm.

Thermal figures of merit	E antenna NFT at 850 nm	E antenna NFT at 1550 nm
$\Delta T_{medium}/\Delta T_{NFT}$	1.83	4.33
Thermal spot size (nm^2)	76×89	75×88
Thermal gradient (K/nm)	7.55: cross track	9.5: cross track
	6.46: down track	3.8: down track
$\Delta T_{medium}/P_{incident}$ (K/mW)	124.3	80

NFTs for 800 and 1550 nm up to the steady state. The NFTs reach a steady state temperature within about 100 ns.

The performance of an E antenna at two different wavelengths and their optical and thermal performance is compared next. Two different E antenna designs, one resonant at 850 nm and another at 1550 nm are studied. The E antenna, resonant at 850 nm has the dimensions of $w = 20$ nm, $l = 50$ nm, $p_1 = 600$ nm, $p_2 = 316$ nm, $q_1 = 300$ nm, and $q_2 = 186$ nm while the E antenna resonant at 1550 nm has the dimensions of $w = 20$ nm, $l = 80$ nm, $p_1 = 1200$ nm, $p_2 = 750$ nm, $q_1 = 200$ nm, and $q_2 = 100$ nm. It is found that the maximum coupling efficiency at 850 nm is 5.8% while it is 3.8% at 1550 nm. The thermal simulation results reveal similar higher ratio of $\Delta T_{medium}/\Delta T_{NFT}$ as in the triangle NFT case, which can be seen in Table III.

Figure 7 shows the temporal temperature rise of the E antenna NFTs for 800 and 1550 nm up to the steady state. From the cross sectional temperature profiles in the inset of Fig. 7, it is clear that the temperature rise of the NFT at
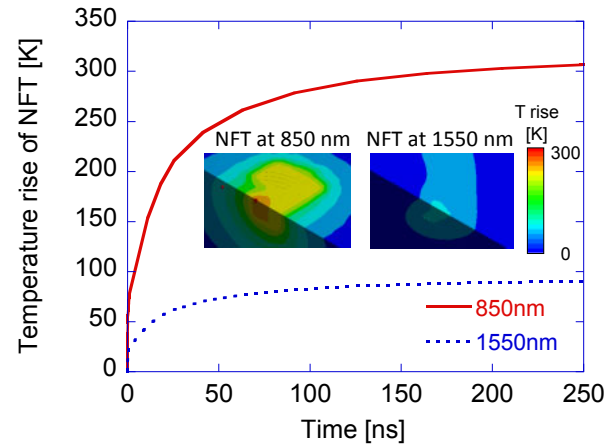
Fig. 7. (Color online) Temporal rise of the peak temperature of the E antenna NFTs at 800 and 1550 nm. Inset shows the cross sectional temperature profiles of the NFTs.

steady state is much less at 1550 nm than at 850 nm. For the same incident power, the temperature rise in the medium is 1.4 times more at 850 nm than at 1550 nm due to the higher coupling efficiency. However, at the same time, the peak temperature rise for the NFT at 850 nm is 3.39 times higher than that at 1550 nm. The thermal figure of merit for the NFT at 1550 nm is 4.33 versus 1.83 for the NFT at 850 nm as given in Table III. The thermal spot size (FWHM) at 1550 nm is 75 nm × 88 nm while that at 850 nm is 76 × 89 nm^2. The thermal spot size or the thermal gradients does not change significantly for the E antenna at longer wavelengths. This is primarily because in the E antenna, the spot size is constrained by the width of the notch, unlike in the case of triangle antenna where the optimized tip geometry changes at longer wavelengths.

4.2 Modified NFT geometry: Introduction of a taper

In this section, we describe another method of improving the NFT performance by making simple modifications in the geometry of the NFT. It has been previously demonstrated that in the case of bowtie apertures as a plasmonic antenna, introduction of a tapered side wall in place of a straight wall results in a higher field concentration and a sub 20 nm spot size.[36] The effect of introduction of the taper of the NFT optical and thermal performance is studied for an E antenna and discussed here.

Figure 8(a) shows the isometric view of an E antenna with a straight walled notch. Figure 8(b) shows the zoomed in view of the notch. Figures 8(c) and 8(d) are derived from the E antenna having a taper in the notch across the axis of the notch and along the axis of the notch, which is denoted by the angle α and θ, respectively.

Figure 9 shows the variation of the coupling efficiency with the angle θ and α for the NFT designs. It is seen that when the angle θ is close to 0°, the coupling efficiency does not vary significantly with the change in the angle α for up to 10 to 15°. For larger values of θ and α, the coupling efficiency falls down. Due to the addition of the tapers, the length and the width of the notch becomes different in the top side and the bottom side which detunes from the resonance condition. But, at the same time, widening of the base of the notch helps in providing more surface charges to the tip of the notch. Combined with these two effects, the coupling
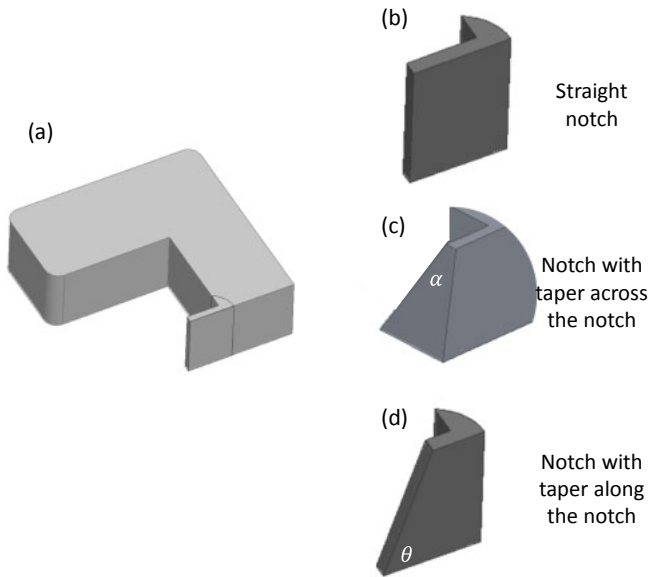
Fig. 8. (Color online) (a) Isometric view of the cross section of an E antenna with straight notch. Zoomed in view of (b) the notch having straight side walls (c) the notch having tapered side walls with the taper angle (α) across the notch and (d) the notch having tapered side walls with the taper along the axis of the notch.
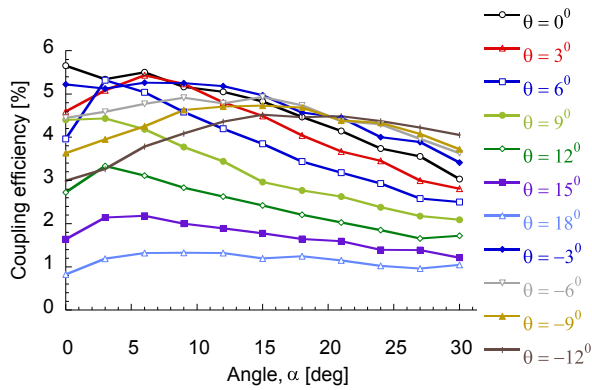

Fig. 9. (Color online) Coupling efficiency with variation of both the taper angles (θ) and (α).

Table IV. Table comparing the thermal performance of E antenna with straight notch and tapered notch.

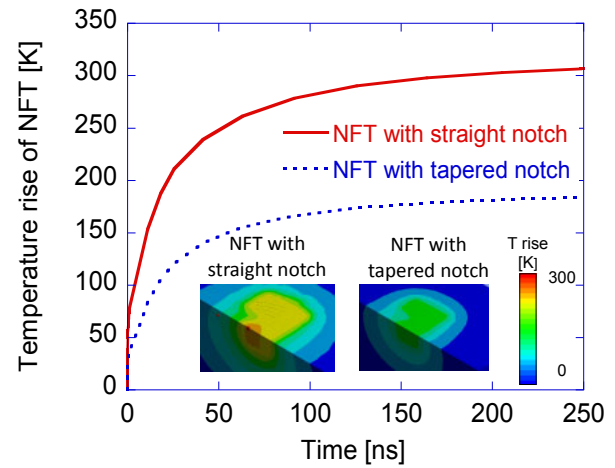| Thermal figures of merit	E antenna with straight notch	E antenna with tapered notch ($\alpha = 14°$ and angle $\theta = 0°$)
$\Delta T_{medium}/\Delta T_{NFT}$	1.83	3.14
Thermal spot size (nm^2)	76×89	64×62
Thermal gradient (K/nm)	7.55: cross track 6.46: down track	5.5: cross track 4.72: down track
$\Delta T_{medium}/P_{incident}$ (K/mW)	124.3	117

Fig. 10. (Color online) Graph showing the temporal rise of the peak temperature of the E antenna NFTs with a straight notch and a tapered notch. Inset shows the cross sectional temperature profiles of the NFT.

between the straight notch and tapered notch designs. The difference in the temperature rise of the NFTs for the straight notch and the tapered notch can also be seen from Fig. 10 which shows the temporal rise of the NFTs up to the steady state and the cross sectional temperature profile of the two antenna designs. Hence, by the suitable design of a tapered side wall, the thermal performance can be significantly enhanced leading to lower NFT self-heating.

It is found that the maximum temperature rise of the NFT reaches 312 K for the E antenna with the straight notch while it is 186 K for the E antenna with the tapered notch. Having a wide base for the tapered notch helps dissipating the heat from the base of the notch and the temperature rise at the notch is much lower. The pyramidal shape of the notch acts a better heat sink which helps in the reduction of the maximum NFT temperature.[37]

5. Conclusion

In this paper, we summarized the optical and thermal performance of several NFT designs for HAMR applications. Different figures of merit were discussed and used for quantifying the NFT functionalities. We also discussed strategies for improving the performance of existing NFTs to improve over the current figures of merit by making a few modifications. It was found that by operating the NFTs in the longer wavelength regime as well as by introducing small tapers can impact the thermal performance of the NFTs and can reduce the peak temperature rise of the NFTs. Hence, these studies point to different directions to improve the performance of an NFT.

efficiency does not show a significant variation. However, since increasing the angle α widens the base of the notch, it should help in dissipating more heat from the notch to the main body of the E antenna thereby reducing the peak temperature rise of the NFT. This effect is illustrated from the results of the thermal simulation shown in the next section.

Table IV summarizes the comparison of the various figures of merit for the straight notch and tapered notch E antennas with $\alpha = 14°$ and $\theta = 0°$. From the tabular data, it is seen that the tapered notch performs significantly better for $\Delta T_{medium}/\Delta T_{NFT}$. The ratio of the temperature rise in the medium to the NFT is 1.7 times better for the tapered notch which means that the temperature rise in the tapered notch NFT would be much smaller in order to raise the temperature of the recording medium to a particular value. The thermal spot size is 64×62 nm^2 for the tapered notch whereas the spot size is 76×89 nm^2 for a straight notch of similar notch dimensions. The thermal gradient in the recording medium and the temperature rise of the medium increases per milliwatt of incident laser power is not affected much

Acknowledgments

1) M. P. Sharrock, IEEE Trans. Magn. 26, 193 (1990).
2) M. H. Kryder, E. C. Gage, T. W. McDaniel, W. A. Challener, R. E. Rottmayer, G. Ju, Y.-T. Hsia, and M. F. Erden, Proc. IEEE 96, 1810 (2008).
3) R. E. Rottmayer, S. Batra, D. Buechel, W. A. Challener, J. Hohlfeld, Y. Kubota, L. Li, B. Lu, C. Mihalcea, and K. Mountfield, IEEE Trans. Magn. 42, 2417 (2006).
4) L. Pan and D. B. Bogy, Nat. Photonics 3, 189 (2009).
5) N. Zhou, X. Xu, A. T. Hammack, B. C. Stipe, K. Gao, W. Scholz, and E. C. Gage, Nanophotonics 3, 141 (2014).
6) M. A. Seigler, W. A. Challener, E. Gage, N. Gokemeijer, G. Ju, B. Lu, K. Pelhos, C. Peng, R. E. Rottmayer, X. Yang, H. Zhou, and T. Rausch, IEEE Trans. Magn. 44, 119 (2008).
7) ASTC Technology Roadmap 2016 [http://idema.org/?page_id=5868] (cited April 19, 2017).
8) E. X. Jin and X. Xu, Jpn. J. Appl. Phys. 43, 407 (2004).
9) K. Tanaka and M. Tanaka, J. Microsc. (Oxford, U.K.) 210, 294 (2003).
10) R. Katayama, T. Kasuya, S. Sugiura, and K. Yoshizawa, Jpn. J. Appl. Phys. 54, 09MG01 (2015).
11) W. A. Challener, E. Gage, A. Itagi, and C. B. Peng, Jpn. J. Appl. Phys. 45, 6632 (2006).
12) W. A. Challener, T. W. McDaniel, C. D. Mihalcea, K. R. Mountfield, K. Pelhos, and I. K. Sendur, Jpn. J. Appl. Phys. 42, 981 (2003).
13) W. A. Challener and A. V. Itagi, in Modern Aspects of Electrochemistry No. 44, ed. M. Schlesinger (Springer, New York, 2009) Chap. 2.
14) A. V. Ermushev, B. V. McHedlishvili, V. A. Oleinikov, and A. V. Petukhov, Quantum Electron. 23, 435 (1993).
15) K. Osawa, K. Sekine, M. Saka, N. Nishida, and H. Hatano, J. Magn. Soc. Jpn. 33, 503 (2009).
16) B. C. Stipe, T. C. Strand, C. C. Poon, H. Balamane, T. D. Boone, J. A. Katine, J.-L. Li, V. Rawat, H. Nemoto, and A. Hirotsune, Nat. Photonics 4, 484 (2010).
17) W. A. Challener, C. B. Peng, A. V. Itagi, D. Karns, W. Peng, Y. Y. Peng, X. M. Yang, X. B. Zhu, N. J. Gokemeijer, Y. T. Hsia, G. Ju, R. E. Rottmayer, M. A. Seigler, and E. C. Gage, Nat. Photonics 3, 220 (2009).
18) N. Zhou, L. M. Traverso, and X. Xu, Nanotechnology 26, 134001 (2015).
19) E. X. Jin and X. Xu, Appl. Phys. Lett. 88, 153110 (2006).
20) X. L. Shi and L. Hesselink, Jpn. J. Appl. Phys. 41, 1632 (2002).
21) K. Şendur, Opt. Express 18, 4920 (2010).
22) T. Matsumoto, F. Akagi, M. Mochizuki, H. Miyamoto, and B. Stipe, Opt. Express 20, 18946 (2012).
23) T. Matsumoto, K. Nakamura, T. Nishida, H. Hieda, A. Kikitsu, K. Naito, and T. Koda, Appl. Phys. Lett. 93, 031108 (2008).
24) B. Xu, Z. Liu, R. Ji, Y. Toh, J. Hu, J. Li, J. Zhang, K. Ye, and C. Chia, J. Appl. Phys. 111, 07B701 (2012).
25) B. Liu and Y. Han, J. Appl. Phys. 93, 8716 (2003).
26) P. Yu, W. Zhou, S. Yu, and Y. Zeng, Int. J. Heat Mass Transf. 59, 36 (2013).
27) L. Wu, Nanotechnology 18, 215702 (2007).
28) H. Li, B. Liu, H. Y. Ye, and T. C. Chong, Jpn. J. Appl. Phys. 44, 7950 (2005).
29) B. X. Xu, C. W. Chia, Q. D. Zhang, Y. T. Toh, C. W. An, and G. Vienne, Jpn. J. Appl. Phys. 50, 09MA05 (2011).
30) Z. Cen, B. Xu, J. Hu, J. Li, K. Cher, Y. Toh, K. Ye, and J. Zhang, Opt. Express 21, 9906 (2013).
31) A. Datta and X. Xu, Opt. Eng. 56, 121906 (2017).
32) A. Datta and X. Xu, IEEE Trans. Magn. 53, 3102105 (2017).
33) L. Wang and X. Xu, Appl. Phys. A 89, 293 (2007).
34) N. Berkovitch, P. Ginzburg, and M. Orenstein, J. Phys.: Condens. Matter 24, 073202 (2012).
35) P. B. Johnson and R.-W. Christy, Phys. Rev. B 6, 4370 (1972).
36) Y. Chen, J. Chen, X. Xu, and J. Chu, Opt. Express 23, 9093 (2015).
37) A. Datta and X. Xu, IEEE Trans. Magn. 52, 3101306 (2016).

Anurup Datta is a Ph.D. student in the department of Mechanical Engineering at Purdue University. He received his B.Tech degree in Manufacturing Science and Engineering from the Indian Institute of Technology, Kharagpur in 2012. His research interests include sub wavelength focusing of light, nano-lithography, and heat assisted magnetic recording. He is a student member of SPIE.

Xianfan Xu is the James J. and Carol L. Shuttleworth Professor of Mechanical Engineering and a professor of Electrical and Computer Engineering (by courtesy) at Purdue University. He obtained his M.S. and Ph.D. degrees in Mechanical Engineering from the University of California, Berkeley in 1991 and 1994, respectively. His research interests include fundamentals of ultrafast laser-matter interaction, near-field nano-optics, and laser-based micro and nano engineering. He is a fellow of SPIE, a fellow of the American Society of Mechanical Engineers (ASME), and a fellow of the Optical Society of America (OSA).